Northumbria Research Link

www.northumbria.ac.uk/nrl

northumbria
UNIVERSITY NEWCASTLE

Surface Stability of Spinel $MgNi_{0.5}Mn_{1.5}O_4$ and $MgMn_2O_4$ as Cathode Materials for Magnesium Ion Batteries

Wei Jin,[1] Guangqiang Yin,[1] Zhiguo Wang,[1*] Y.Q. Fu[2*]

1 *School of Physical Electronics, University of Electronic Science and Technology of China, Chengdu, 610054, P.R. China*

2 *Department of Physics and Electrical Engineering, Faculty of Engineering and Environment, University of Northumbria, Newcastle upon Tyne, NE1 8ST, UK*

[*]Corresponding author. E-mail: zgwang@uestc.edu.cn (ZW); richard.fu@northumbria.ac.uk (YQF)

ABSTRACT

Rechargeable ion batteries based on the intercalation of multivalent ions are attractive due to their high energy density and structural stability. Surface of cathode materials plays an important role for the electrochemical performance of the rechargeable ion batteries. In this work we calculated surface energies of (001), (110) and (111) facets with different terminations in spinel $MgMn_2O_4$ and $MgNi_{0.5}Mn_{1.5}O_4$ cathodes. Results showed clearly that atomic reconstruction occurred due to surface relaxation. The surface energies for the (001), (110) and (111) surfaces of the $MgNi_{0.5}Mn_{1.5}O_4$ were 0.08, 0.13 and 0.11 J/m^2, respectively, whereas those of the Ni-doped $MgMn_2O_4$ showed less dependence on the surface structures.

Keywords: Surface stability, Mg ion batteries, Density functional theory

1. Introduction

Currently, the electrode materials for rechargeable ion batteries based on the intercalation of multivalent ions are attractive for their high energy density and structural stability [1-3]. The research is now focused on finding suitable electrode materials with a good electrochemical performance for magnesium ion batteries (MIBs) in order to achieve high energy capacity and safety rechargeable ion batteries for electric vehicles [4-11]. Oxides with a spinel structure such as spinel-type Mn_2O_4 are widely used as cathode materials for lithium ion batteries (LIBs) [12, 13]. Actually spinel-type $LiMn_2O_4$ has been used as the cathode materials of the LIBs in electric vehicles [14, 15]. However, the commercial development of the $LiMn_2O_4$ (LMO) is hindered by several drawbacks including a severe capacity degradation during cycling due to a Jahn-Teller (JT) distortion, as well as dissolution of Mn in the electrolyte. Doping with other transitional metal elements into the LMO can improve the electrochemical performance of the LIBs. Among them doping with Ni could make the spinel structure LMO more stable, thus improving the circulation characteristics of the LIBs [16, 17]. Amine et al. [18] reported that the $LiNi_{0.5}Mn_{1.5}O_4$ (LNMO) used as the cathode material for LIBs presented high discharge capacity and good cyclic reversibility.

Intercalation of Mg^{2+} ions instead of Li^+ ions into a spinel-type Mn_2O_4 could be used in fabricating a cathode material for the MIBs. This has attracted much attention since the MIBs can provide a higher volumetric energy density and a lower cost as Mg^{2+} ions carry two charges per ion, and the charge storage capability is twice as much as that of Li^+ ions at the same concentration. Yuan et al. [2] reported that λ-MnO_2 showed a high specific capacity and good coulombic efficiency in a $MgCl_2$ electrolyte. A large discharge specific capacity of 545.6

mAh g^{-1} was achieved in 0.5 mol dm^{-3} $MgCl_2$ at a current density of 13.6 mA g^{-1}, together with a high columbic efficiency of ~100% [2]. Kim et al. [3] investigated the reversibility of Mg intercalation into the spinel-type Mn_2O_4 using a scanning transmission electron microscope, and provided a direct visualization of electrochemical intercalation of Mg^{2+} into the tetrahedral sites of a spinel oxide host. Kim et al. [11] claimed that the electrode composed of λ-MnO_2 has a higher discharging capacity and a better efficiency for the insertion/desertion of the Mg ions when compared with those of α-MnO_2 in the first cycle, but exhibited a poor capacity retention of 57% after the fifth cycle. It is generally agreed that nanoscale electrode materials have advantages to allow a fast Li diffusion, show a better accommodation of the strains during lithium insertion/removal, and thereby improve the cycle life of the LIBs [19]. The dramatically increased electrode/electrolyte contact areas due to using the nanostructured LIBs lead to higher charge/discharge rates, shorter path lengths for electronic transport (permitting operation with a low electronic conductivity or at a higher power) and shorter path lengths for Li ion transport (permitting operation with a low Li ion conductivity or at a higher power) [19]. Superior rate capability in nanostructured $LiNi_{0.5}Mn_{1.5}O_4$ has been reported [20]. The surface stability is important for the nano-scale electrode materials to be used [21, 22], Surface modifications by carbon materials, AlF_3, nano-Y_2O_3, TiO_2 and Al_2O_3 coatings have been used to improve the electrochemical performance of the $LiNi_{0.5}Mn_{1.5}O_4$ [23-26]. As the valence of Mg ions is higher than that of Li ions, the valence of Mn in $MgMn_2O_4$ (MMO) must decrease from average 3.5^+ to 3^+ to keep the charge neutrality. The JT distortion occurs due to the presence of high spin Mn^{3+} ions in the MMO. By replacement of part of the Mn with Ni, some Mn can keep at a state of 4^+, thus avoiding the JT distortion, as discussed in the

section of results of this paper. From the superior rate capability of the LNMO [20], in this paper we used a doping level of 0.5 in the $MgNi_{0.5}Mn_{1.5}O_4$ (MNMO) to investigate the doping effect on the surface stability of the MMO. The optimal doping level is needed to verify from theoretical and experimental confirmation. Considering the importance of surface structure and stability of the MMO and MNMO as cathode materials for the MIBs, in the present work, we investigated surface stability of both the MMO and MNMO using density functional theory (DFT). All the possible terminations of low-index (001), (110) and (111) facets on the MMO and MNMO were discussed.

2. Simulation details

All the calculations were performed using the SIESTA code [27, 28] within a generalized gradient approximation (GGA) using the Perdew-Burke-Ernzerhof (PBE) functional [29]. The interactions between the core electrons and valence electrons were described by nonlocal norm-conserving pseudo-potentials [30]. Simply employing the GGA is insufficient to capture the correct electronic state of materials. GGA+U can improve the description of the electronic structure. Karim et al. investigated the surface properties of $LiMn_2O_4$ spinel using the GGA and GGA+U for the electron exchange-correlation function [31]. They found that although the surface energies derived in the GGA and GGA+U differ by the absolute values, but the resulting Wulff shape obtained using these two is comparable due to their similar relative surface energies [31]. Therefore, we expected the omission of the Hubbard-type correction in our work would not significantly affect our conclusion. The valence electron wave functions were expanded using double-ζ basis functions. The lattice parameters and atom positions were

all allowed to relax by using a conjugate gradient minimization with a target pressure of 0 GPa and the residual forces on each atom were smaller than 0.02 eV/Å on each atom. For calculating the self-consistent Hamiltonian matrix elements, the charge density was projected on a real space grid with a cutoff of 180 Ry. The localization radii of the basis function were determined using an energy shift of 0.01 Ry. The split norm used was 0.16. During the simulations a linear mixing strategy [32] was used where the input density matrix for the (n+1) stage of the self-consistent cycle was: $\rho_{in}^{n+1} = \alpha\rho_{out}^{n} + (1-\alpha)\rho_{in}^{n}$. Density mixing weight of 0.01 was used in this work. An 4×4×4 Monkhorst-Pack mesh [33] was used for the k-points sampling of the Brillouin zone integration. Spin-polarization was considered for all the simulations.

Recently, it was reported that the standard DFT with (semi)-local exchange correlation functional is not sufficient to describe the structural changes in cathode materials [34, 35]. Combining the DFT+U calculation and the van der Waals (vdW) interactions can yield more accurate lithiation voltages, relative stabilities, and structural properties which are in better agreement with experimental values in a layered cathode Li_xCoO_2 [34]. The vdW interactions help to stabilize inserted ions and contribute to hinder ion diffusion in a layered V_2O_5 [36]. From the results of Scivetti et al. [37], the vdW interactions do not affect relative stability of (001)-Li terminated surface and the (111)-Mn/Li-terminated surface in the spinel LNMO. Therefore, we expected the omission of the vdW interactions in our work would not significantly affect our conclusion.

Crystal structures of the MMO and MMNO are shown in Fig. 1. The simulation supper cells of both the MMO and MNMO are consisted of 56 atoms. The skeleton of spinel-Mn_2O_4

in the $MgMn_2O_4$ (shown in Fig. 1(a)) is a three-dimensional network with tetrahedral and octahedral coplanar structures. Therefore, oxygen atoms were accumulated closely as in the face-centered cubic structure, and 75% of Mn atoms were alternately located among cubic close packing oxygen layers. The remaining Mn atoms were located in the adjacent layers. There were still plenty of Mn ions existed in each layer to keep the oxygen an ideal state for a cubic close packing, and ions were directly embedded in the tetrahedral gaps of oxygen atoms. This type of three-dimensional tunnel structure is more advantageous than the interlayer shape for insertion/extraction of the Mg ions. As shown in Fig. 1(b), Mg, Mn and Ni in spinel-type $MgNi_{0.5}Mn_{1.5}O_2$ occupy 8c, 4b and 12d sites, respectively; O atoms occupy the 8c and 24e sites. Before the calculation of surface energies, the unit cells of the MMO and MNMO were all optimized. According to the periodic arrangement, all the possible terminations for (001), (110) and (111) facets were considered, i.e. two types of (001) and (110) terminations for both the MMO and MNMO, six types of (111) terminations for the MMO and MNMO, respectively. Using periodic boundary conditions for the repeated slab model calculations, the slabs were separated at least 25 Å in order to avoid the periodic image interactions.

The surface energy E_{surf} was calculated using the following equation [38].

$$E_{surf} = E_{cl} + E_{rel} \qquad (1)$$

where E_{cl} is the cleavage energy of complementary surface, which can be calculated for the unrelaxed slabs using Eq.(2).

$$E_{cl}(A+B) = \left[E_{unrel}(A) + E_{unrel}(B) - nE_{bulk} \right] / 4S \qquad (2)$$

where $E_{unrel}(A)$ and $E_{unrel}(B)$ represent the total energies of unrelaxed A- and B-terminated slabs, respectively. A and B-terminated surfaces are mutually complementary; S is the area of

the A- and B- terminated surface, and E_{bulk} is the energy of corresponding bulk materials per formula units; n is the number of formula units in the A and B-terminated slabs. E_{rel} is the relaxation energy for each of the surfaces, which can be calculated using Eq.(3).

$$E_{rel}(a) = \left[E_{rel}(A) - E_{unrel}(A)\right] / 2S \qquad (3)$$

Here $E_{rel}(a)$ is the relaxation energy of the A-terminated surface, $E_{rel}(A)$ is the total energy of A-terminated slab after relaxation, and $E_{unrel}(A)$ is the total energy of unrelaxed A-terminated slab.

3. Results and discussion

The unit cell of the MNMO contains 8 Mg atoms, 32 O atoms and 16 Ni+Mn atoms. All the possible variations of randomly distributed Mn and Ni in the unit cell are tested, as shown in Fig. 1 (a) and Table 1. The sequence of number of metals in the Table 1 has been marked in Fig. 1 (a), and the calculated relative energies reference to the lowest energy is shown in Table 1. Results show that the most stable structure is when the Ni and Mn ions are regularly ordered and occupy 4b and 12d, respectively. The subsequent bulk and surface calculations of the MNMO were based on this configuration, as shown in Fig. 1(b).

Both ferromagnetic (FM) ordering [39] and antiferromagnetic (AFM) [40] orderings along the [110] direction with alternating spin up and down (↑↓↑↓) were tested for both the bulk MMO and MNMO. The calculated lattice constants of the bulk MMO relaxation with an FM ordering spin are: $a=b=c=8.56$ Å with a cubic symmetry ($\alpha=\beta=\gamma= 90°$), while the JT distortion occurs along the z direction after the bulk MMO relaxation with an AFM ordering spin ($a=8.31$, $b=8.31$, $c=9.10$ Å, $\alpha=\beta=\gamma= 90°$). These results agree with that for the LMO [41].

After replacing Mn with Ni in the MMO, the structure of the MNMO can keep the cubic symmetry calculated either using the FM or AFM, indicating that the JT distortion can be effectively constrained by substituting Mn with Ni. The calculated lattice constants are listed in Table 2. The results of Kim *et al.* [41] also showed that the AFM or FM ordering does not have a considerable effect on the surface energies of (001) surface of the LNMO. Therefore, only the FM ordering spin was considered for the rest simulations of this work.

Building stoichiometric slabs with symmetrically equivalent surfaces and relaxing all atoms of the slabs, proved by Kim *et al.* [41], were the fastest converging scheme in calculating the surface energies. Fig. 2 shows the dependence of surface energies on the slab thickness. The variation of surface energy differs for different orientation surfaces with different terminations. The surface energies of Mn/O-terminated (001) surface of MMO and Ni/Mn/O-terminated (001) surface of MNMO decrease as the slab thickness increases. From the figure, all the surface energies are converged to given values as the thickness of slab increases. The number of atoms used for calculating the values in this work are given in Table 2, which is sufficient to obtain accurate surface energies.

The MNMO is composed of Mg- and Ni/Mn/O- atomic layers alternatively along the [001] crystal orientation, as shown in Fig. 3(a). Therefore, there are two types of terminations for the (001) surfaces, i.e. Mg- and Ni/Mn/O- atomic layers. The Mg- and Mn/Ni/O-terminated surfaces are complementary mutually along the [001] crystal orientation. There are also two types of terminations for the (001) surfaces in the MMO, i.e. Mg- and Mn/O- atomic layers as shown in Fig. 3(b). The MNMO is stacked with sequences of Mn/O-, Mg/Ni/Mn/O(I), Ni/Mn/O-, and Mg/Ni/Mn/O(II) atomic layers along the [110] crystal orientation, as shown in

Fig. 3(c). Therefore, there are four types terminations for the (110) surfaces in the MNMO, i.e. Mn/O-, Mg/Ni/Mn/O(I)-, Ni/Mn/O-, and Mg/Ni/Mn/O(II)- atomic layers. Fig. 3(d) shows that there are only two types of terminations for the (110) surfaces in the MMO, i.e. Mn/Ni- and Mg/Mn/O-layers. As shown in Figs. 3(e) and 2(f), there are six types of terminations for both the MNMO and MMO along [111] crystal orientation. The configuration of the atomic layers of the MNMO has the periodical sequences, i.e. in the order of Mn/Ni(I)-, O(I)-, O(II)-, Mg(I)-, Mn/Ni(II)- and Mg(II) atomic layers as shown in Fig. 3 (e). The O(I)- and O(II)- terminations have the same atomic layer structure but different adjacent atomic layers which may lead to the different surface stabilities. Similarly, the surfaces terminated with Mg(I)- and Mg(II)-layers have the same atomic configuration but different adjacent atomic layers. The Mn/Ni(I)-terminated surfaces are consisted of nine Mn atoms and three Ni atoms, and have different atomic layer structures with Mn/Ni(II)-terminated surfaces, which have three Mn atoms and one Ni atom in the plane.

As the bonding environment of the surface atoms is different with that in the counterpart one in the bulk materials, thus surface reconstructions often occur, which affect the properties of materials [42-44]. The atoms are frequently arranged periodically on a two-dimensional surface, but the periodicity is often broken in the direction perpendicular to the surface. The calculated surface energies for (001), (110) and (111) facets with different terminations are summarized in Table 3. The surface energies are 0.08 and 0.11 J/m^2 for the (001) surfaces terminated with Mg- and Mn/Ni/O-layers, respectively. For the (001) surface terminated with Mg-layer, the surface Mg atoms move to the second Mn/Ni/O layer perpendicular to the surface after relaxation, as shown in Figs. 4(a) and 4(b). Whereas for the (001) surface

9

terminated with Mn/Ni/O-layer, the outmost Mn/Ni/O-layer moves inward towards the second layer after relaxation. The distances between the first layer and second layer are 1.17 and 0.95Å before and after relaxation, respectively. The same surface relaxation has been observed on (001) surfaces of the MMO. The surface energy values of the (001) surface of MMO terminated with Mg- and Mn/O-layers are 0.08 and 0.10 J/m^2, respectively. For the (001) surface of the MMO terminated with a Mg-layer, the Mg atoms on the surface move to the second Mn/O layer perpendicularly to the surface after relaxation, whereas those on the (001) surface terminated with Mn/O-layer move to the second Mg-layers after relaxation. The distance between the first layer and second layer decreases from 1.17 to 1.03 Å after relaxation, as listed in Table 4.

The (110) surfaces of the MNMO show less dependence on the terminations. The surface energies are close to 0.13 J/m^2. There are no prominent changes of the surface atomic configurations except for the shortening of interlayer distance between the first and second atomic layers after relaxation. The ions on the (110) surface terminated with the Mn/O-layer move closer to the second layer and the interlayer spacing between the first layer and second layer decreases from 1.59 to 1.49 Å after relaxation. For the (110) surface terminated with Mg/Mn/Ni/O(I)-layer, the distances are 1.41 and 1.37 Å before and after relaxation, respectively. In addition, for the MNMO (110) surfaces terminated with Mn/Ni/O- and Mg/Mn/Ni/O(II), the interlayer distance between the first and second atomic layers after relaxation was shorten with ~0.1 Å. The same surface relaxation occurs for the MMO (110) surfaces. The surface energies of (110) facets terminated with Mg- and Mg/Mn/O are both 0.13 J/m^2. The (110) surface of MMO terminated with Mn/O-layer has no obvious change

except the decrease of the distance between the first and second atomic layers from 1.60 to 1.44 Å. The distances between the first and second atomic layers for the (110) surface terminated with Mg/Mn/O-layer are 1.42 and 1.37 Å before and after relaxation, respectively.

The surface energy is not only related to the atomic configuration of terminated surface, but also depends on the sublayer. The surface energies of Mg(I)- and Mg(II)-terminations for the MNMO (111) surface are 0.22 and 0.12 J/m^2, respectively. They have the same atomic configuration but different adjacent atomic layers. For the (111) surface with Mg(I)-teimination, the surface Mg atoms and the second Mn/Ni layer keep intact after relaxation, whereas the third Mg atomic layer moves inward to the fourth O-layer perpendicular to the surface (shown in Figs. 4(c) and 4(d)). The MNMO (111) surface terminated by Mg(II)-layer moves closer to the sublayers after relaxation. The distances between the first and second layers for the (111) surface terminated with Mg(II)-layer are 0.64 and 0.54 Å before and after relaxation, respectively. The surface energies of the (111) facet terminated with O(I)- and O(II)-layers are 0.25 and 0.19 J/m^2, respectively. The different adjacent atomic layers of O(I)- and O(II)-terminations would be a major factor for surface energies difference. For the (111) surface with O(I)-termination, the surface atoms maintain previous configuration after the relaxation, whereas the second atomic layer moves to the third layer perpendicular to the surface, as shown in Figs. 4(e) and 4(f). Nevertheless, the O(II)-terminated surface has no obvious change except the decrease of the distance between the first and second atomic layers from 1.21 to 0.95 Å.

It is worth mentioning that the (111) Mn/Ni(II)-terminated surface shows the lowest surface energy of 0.11 J/m^2 in all possible terminations of the (111) facets. The

Mn/Ni(I)-terminated surface (consisted of nine Mn atoms and three Ni atoms) has different atomic layer structure with that of the Mn/Ni(II)-terminated surface which has three Mn atoms and one Ni atom. In addition, they have different adjacent sublayers. The Mn/Ni(I)-terminated surface is near O-layer, whereas the Mn/Ni(II)-terminated one is adjacent to the Mg-layer. The (111) surface terminated with Mn/Ni(I)-layer moves near to the second atomic Mg-layer after relaxation, and the distances are 1.04 and 1.02 Å before and after relaxation, respectively. However, the surface atoms remain largely intact after relaxation for the (111) surface terminated with the Mn/Ni(II)-layer, whereas the second Mg atomic layer moves inward to the third O-layer perpendicular to the surface which is apparently different from the above results of the (001) and (110) surfaces as shown in Figs. 4(g) and 4(h).

The same surface relaxation occurs for the MMO (111) surfaces. The (111) surfaces of the MMO terminated with Mn(II)-layer and Mg(II)-layer have the lowest surface energy of 0.11 J/m^2, as listed in Table 3. The MMO (111) surfaces terminated by Mn(I)-, O(II)- and Mg(II) show no prominent changes except for the shortening of distance between the first and second atomic layers after relaxation. The distances between the first and second layers of Mn(I)-terminated surfaces are 1.03 and 1.02 Å before and after relaxation. The distances between the first and second layers for the O(II)-terminated surface are 1.23 and 0.84 Å before and after relaxation, respectively. The interlayer distance between the first and second atomic layers of the Mg(II)-terminated surface after relaxation shortens with ~ 0.1 Å. The surface atoms maintain previous configuration after the relaxation, but the second atomic layer moves to the third layer perpendicular to the surface for the (111) surface terminated with O(I)-layer.

For the (111) surface terminated with Mg(I) layers on, the first Mg- and the second Mn-layers keep intact after relaxation, whereas the third Mg atomic layer moves inward to the fourth O-layer perpendicular to the surface. In addition, for the (111) surface terminated with the Mn(II)-layers, the surface atoms remain largely intact after the relaxation, whereas the second atomic layer moves to the third layer perpendicular to the surface.

In general, the results exhibit that the (001) surfaces of both the MMO and MNMO terminated with Mg-layer have the lowest energy values (0.08 J/m^2). For the MNMO, the surface energies of (111) facets terminated with Mn/Ni(II)- and Mg(II) are 0.11 and 0.12 J/m^2 which are very close to the lowest energies of (001) facet. The (111) surfaces terminated by Mn/Ni(II) show the lower surface energy and more stable structure. Compared with the surface energies of the MNMO with those of the MMO, the surface energies show less dependence on the Ni-doping. The Wulff shape of the LMO depends on the surface energy ratio of (001) and (111) surfaces, which varies from truncated-cube to cubo-octahedron to truncated-octahedron shape [41]. Our calculations show that the (001) surface is only 0.03 J/m^2 more stable than the (111) surface, so both the MMO and MNMO show more (001) facets, i.e., with more cubic characters. These results need further experimental confirmations.

Doping with other cations in the LMO may affect the distribution of ions near the surface and in the bulk, thus influencing the structural and electrochemical properties. Recently, compositional segregation of Ni to surfaces in the layered LNMO has been reported [45, 46]. In contrast with the layered-LNMO, a uniform distribution of Ni dopant in a spinel-LNMO has been observed [47], however the Cr, Fe, and Ga dopants have a tendency to segregate toward the surfaces [48]. In order to determine whether the Ni dopant prefers to

segregate at the surface or not, we calculated the formation energy of a Ni atom replacement of a Mn atom in the MMO slabs with stable surface. The formation energy was calculated using [49],

$$E_f(Ni_{Mn}) = E_{tot}(Ni_{Mn}) - E_{tot}(perfect) + \mu_{Mn} - \mu_{Ni} \tag{1}$$

where $E_{tot}(Ni_{Mn})$ and $E_{tot}(perfect)$ are the total energies of a supercell with and without a Mn atom replaced by Ni, respectively. μ_{Mn} and μ_{Ni} are the corresponding chemical potential of bulk Mn and Ni, respectively. The calculated formation energies are shown in Fig. 5. For the substitutional defects in (001) surface terminated with Mg and (110) surface terminated with Mg/Mn/O, the formation energies at the surface are higher than those in the inside, indicating the Ni prefers to occupy Mn site at the inside of slabs. For the (111) surface terminated with Mn(II), the formation energies show less dependence of the position. It can be concluded that Ni is less tendency for segregation at the surface of MMO, which shows the same behavior of spinel-LNMO [47].

Mn dissolution is believed to be the main cause of capacity degradation of the $LiMn_2O_4$ [50-52], which is also responsible for the charge capacity fading of MnO_2 used as cathode of MIBs [8]. In order to solve this problem, surface modification of the cathode electrode is an effective way to reduce the side reactions. It was reported that the single-layer graphene can suppress Mn dissolutions of LMO cathode [53] by blocking Mn diffusion and the oxidation state of surface Mn. Mn dissolution is a possible problem for the usage of MMO and MNMO as cathode for MIBs. To reveal the dissolution process of the MMO and MNMO surface, rare-event simulations such as DFT with blue moon ensemble [54] are needed to simulate the atomic-scale processes involved in the aqueous dissolution.

4. Conclusion

The surface energies of spinel-MNMO and MMO were studied using density functional theory. The result exhibits that the (001) surfaces with Mg-terminations for both MMO and MNMO have the lowest surface energies (0.08 J/m^2). The surface energies of Mn/Ni(II)-terminations surfaces for MNMO (111) facets are 0.11 J/m^2. Two types of surface reconstructions were identified, through either shortening of interlayer distance between the first and second atomic layers or moving of surface atoms into the second layers perpendicular to the surface.

References:

[1] G.G. Amatucci, F. Badway, A. Singhal, B. Beaudoin, G. Skandan, T. Bowmer, I. Plitza, N. Pereira, T. Chapman, R. Jaworski, Investigation of yttrium and polyvalent ion intercalation into nanocrystalline vanadium oxide, J. Electrochem. Soc. 148 (2001) A940-A950.

[2] C. Yuan, Y. Zhang, Y. Pan, X. Liu, G. Wang, D. Cao, Investigation of the intercalation of polyvalent cations (Mg^{2+}, Zn^{2+}) into λ-MnO_2 for rechargeable aqueous battery, Electrochim. Acta 116 (2014) 404-412.

[3] C. Kim, P.J. Phillips, B. Key, T. Yi, D. Nordlund, Y.S. Yu, R.D. Bayliss, S.D. Han, M. He, Z. Zhang, A.K. Burrell, R.F. Klie, J. Cabana, Direct observation of reversible magnesium ion intercalation into a spinel oxide host, Adv. Mater. 27 (2015) 3377-3384.

[4] E. Levi, Y. Gofer, D. Aurbach, On the way to rechargeable Mg batteries: the challenge of new cathode materials, Chem. Mater. 22 (2010) 860-868.

[5] Y.L. Liang, R.J. Feng, S.Q. Yang, H. Ma, J. Liang, J. Chen, Rechargeable Mg batteries with graphene-like MoS_2 cathode and ultrasmall Mg nanoparticle Anode, Adv. Mater. 23 (2011) 640-643.

[6] T.S. Arthur, N. Singh, M. Matsui, Electrodeposited Bi, Sb and $Bi_{1-x}Sb_x$ alloys as anodes for Mg-ion batteries, Electrochem. Commun. 16 (2012) 103-106.

[7] S. Rasul, S. Suzuki, S. Yamaguchi, M. Miyayama, High capacity positive electrodes for secondary Mg-ion batteries, Electrochim. Acta 82 (2012) 243-249.

[8] R. Zhang, X. Yu, K.W. Nam, C. Ling, T.S. Arthur, W. Song, A.M. Knapp, S.N. Ehrlich, X.Q. Yang, M. Matsui, α-MnO$_2$ as a cathode material for rechargeable Mg batteries, Electrochem. Commun. 23 (2012) 110-113.

[9] T. Kaewmaraya, M. Ramzan, J.M. Osorio-Guillen, R. Ahuja, Electronic structure and ionic diffusion of green battery cathode material: Mg$_2$Mo$_6$S$_8$, Solid State Ionics 261 (2014) 17-20.

[10] X.L. Hu, W. Zhang, X.X. Liu, Y.N. Mei, Y. Huang, Nanostructured Mo-based electrode materials for electrochemical energy storage, Chem. Soc. Rev. 44 (2015) 2376-2404.

[11] J.-S. Kim, W.-S. Chang, R.H. Kim, D.Y. Kim, D.W. Han, K.H. Lee, S.S. Lee, S.G. Doo, High-capacity nanostructured manganese dioxide cathode for rechargeable magnesium ion batteries, J. Power Sources 273 (2015) 210-215.

[12] K.A. Gummow R, Thackery M, Improve capacity retention in rechargeable 4V lithium/lithium manganese oxide (spinel) cells, Solid State Ionics 69 (1994) 59-67.

[13] G. Singh, S.L. Gupta, R. Prasad, S. Auluck, R. Gupta, A. Sil, Suppression of Jahn–Teller distortion by chromium and magnesium doping in spinel LiMn$_2$O$_4$: A first-principles study using GGA and GGA+U, J. Phys. Chem. Solids, 70 (2009) 1200-1206.

[14] C. Ling, F. Mizuno, Phase Stability of post-spinel compound AMn$_2$O$_4$(A=Li, Na, or Mg) and its application as a rechargeable battery cathode, Chem. Mater. 25 (2013) 3062-3071.

[15] C.W. Kwo Young, Le Yi Wang, Kai Strunz, Electric vehicle battery technologies, in: G.V. Rodrigo, A.P.L. João (Eds.), Electric Vehicle Integration into Modern Power Networks, Springer, 2013, pp. 15-56.

[16] Z.M. Yu, L.C. Zhao, Preparation and electrochemical properties of LiMn$_{1.95}$M$_{0.05}$O$_4$ (M=Cr, Ni), Rare Metals 26 (2007) 62-67.

[17] J. Shu, T.F. Yi, M. Shui, Y. Wang, R.-S. Zhu, X.F. Chu, F. Huang, D. Xu, L. Hou, Comparison of electronic property and structural stability of LiMn$_2$O$_4$ and LiNi$_{0.5}$Mn$_{1.5}$O$_4$ as cathode materials for lithium-ion batteries, Comp. Mater. Sci. 50 (2010) 776-779.

[18] H.T. K. Amine, H. Yasuda, and Y. Fuiita, A new three-volt spinel Li$_{1+x}$Mn$_{1.5}$Ni$_{0.5}$O$_4$ for secondary lithium batteries, J. Electrochem. Soc. 143 (1997) 1607-1613.

[19] P.G. Bruce, B. Scrosati, J.M. Tarascon, Nanomaterials for rechargeable lithium batteries, Angew. Chem. Int. Edit. 47 (2008) 2930-2946.

[20] X. Zhang, F. Cheng, J. Yang, J. Chen, LiNi$_{0.5}$Mn$_{1.5}$O$_4$ porous nanorods as high-rate and long-life cathodes for Li-ion batteries, Nano Letters 13 (2013) 2822-2825.

[21] A. Karim, S. Fosse, K.A. Persson, Surface structure and equilibrium particle shape of the LiMn$_2$O$_4$ spinel from first-principles calculations, Phys. Rev. B 87 (2013) 075322.

[22] E. Lee, K.A. Persson, Corrigendum: First-principles study of the nano-scaling effect on the electrochemical behavior in LiNi$_{0.5}$Mn$_{1.5}$O$_4$, Nanotechnology 25 (2014) 159501.

[23] H. Wang, Z. Shi, J. Li, S. Yang, R. Ren, J. Cui, J. Xiao, B. Zhang, Direct carbon coating at high temperature on LiNi$_{0.5}$Mn$_{1.5}$O$_4$ cathode: Unexpected influence on crystal structure and electrochemical performances, J. Power Sources 288 (2015) 206-213.

[24] Q. Wu, Y. Yin, S. Sun, X. Zhang, N. Wan, Y. Bai, Novel AlF$_3$ surface modified spinel LiMn$_{1.5}$Ni$_{0.5}$O$_4$ for lithium-ion batteries: performance characterization and mechanism exploration, Electrochim. Acta 158 (2015) 73-80.

[25] W.C. Wen, X.K. Yang, X.Y. Wang, L.G.H. Shu, Improved electrochemical performance of the spherical LiNi$_{0.5}$Mn$_{1.5}$O$_4$ particles modified by nano-Y$_2$O$_3$ coating, J. Solid State Electr. 19 (2015) 1235-1246.

[26] H.M. Cho, M.V. Chen, A.C. MacRae, Y.S. Meng, Effect of surface modification on nano-structured LiNi$_{0.5}$Mn$_{1.5}$O$_4$ spinel materials, ACS Appl. Mater. Inter. 7 (2015) 16231-16239.

[27] T. Slusarski, B. Brzostowski, D. Tomecka, G. Kamieniarz, Application of the package SIESTA to linear

models of a molecular chromium-based ring, Acta Phys. Pol. A 118 (2010) 967-968.

[28] F. Yndurain, First-principles calculations of the diamond (110) surface: a mott insulator, Phys. Rev. B 75 (2007) 195443.

[29] M. Liu, Z. Rong, R. Malik, P. Canepa, A. Jain, G. Ceder, K.A. Persson, Spinel compounds as multivalent battery cathodes: a systematic evaluation based on ab initio calculations, Energy Environ. Sci. 8 (2015) 964-974.

[30] N. Troullier, J.L. Martins, Efficient pseudopotentials for plane-wave calculations, Phys. Rev. B 43 (1991) 1993-2006.

[31] A. Karim, S. Fosse, K.A. Persson, Surface structure and equilibrium particle shape of the $LiMn_2O_4$ spinel from first-principles calculations, Phys. Rev. B 87 (2013) 075322.

[32] M.S. José, A. Emilio, D.G. Julian, G. Alberto, J. Javier, O. Pablo, S.-P. Daniel, The SIESTA method for ab initio order- N materials simulation, J.Phys-Condens. Mat. 14 (2002) 2745.

[33] R.A. Evarestov, V.P. Smirnov, Modification of the Monkhorst-Pack special points meshes in the Brillouin zone for density functional theory and Hartree-Fock calculations, Phys. Rev. B, 70 (2004) 233101.

[34] M. Aykol, S. Kim, C. Wolverton, van der Waals interactions in layered lithium cobalt oxides, J. Phys. Chem. C 119 (2015) 19053-19058.

[35] S. Kim, J.K. Noh, M. Aykol, Z. Lu, H. Kim, W. Choi, C. Kim, K.Y. Chung, C. Wolverton, B.W. Cho, Layered-layered-spinel cathode materials prepared by a high-energy ball-milling process for lithium-ion batteries, ACS Appl. Mater. Inter. 8 (2016) 363-370.

[36] J. Carrasco, Role of van der Waals forces in thermodynamics and kinetics of layered transition metal oxide electrodes: alkali and alkaline-earth ion insertion into V_2O_5, J. Phys. Chem. C 118 (2014) 19599-19607.

[37] I. Scivetti, G. Teobaldi, (Sub)surface-promoted disproportionation and absolute band alignment in high-power $LiMn_2O_4$ cathodes, J. Phys. Chem. C 119 (2015) 21358-21368.

[38] J. Cui, W. Liu, First-principles study of the (001) surface of cubic $BiAlO_3$, Physica B 405 (2010) 4687-4690.

[39] R. Benedek, M.M. Thackeray, Simulation of the surface structure of lithium manganese oxide spinel, Phys. Rev. B 83 (2011) 195439.

[40] C.Y. Ouyang, X.M. Zeng, Ž. Šljivancanin, A. Baldereschi, Oxidation states of Mn atoms at clean and Al_2O_3-covered $LiMn_2O_4(001)$ surfaces, J. Phys. Chem. C 114 (2010) 4756-4759.

[41] S. Kim, M. Aykol, C. Wolverton, Surface phase diagram and stability of (001) and (111) $LiMn_2O_4$ spinel oxides, Phys. Rev. B, 92 (2015) 115411.

[42] L. Vitos, J. Kollar, H.L. Skriver, Full charge-density calculation of the surface-energy of metals, Phys. Rev. B, 49 (1994) 16694-16701.

[43] L. Vitos, A.V. Ruban, H.L. Skriver, J. Kollar, The surface energy of metals, Surf. Sci. 411 (1998) 186-202.

[44] Y.Y. Andreev, A.E. Kutyrev, Calculation of the surface gibbs energy and the equilibrium concentration vacancies in the surface layer of BCC metals, Russ. J. Phys. Chem. 75 (2001) 609-614.

[45] M. Gu, I. Belharouak, A. Genc, Z. Wang, D. Wang, K. Amine, F. Gao, G. Zhou, S. Thevuthasan, D.R. Baer, J.G. Zhang, N.D. Browning, J. Liu, C. Wang, Conflicting roles of nickel in controlling cathode performance in lithium ion batteries, Nano Letters 12 (2012) 5186-5191.

[46] M. Gu, A. Genc, I. Belharouak, D. Wang, K. Amine, S. Thevuthasan, D.R. Baer, J.G. Zhang, N.D. Browning, J. Liu, C. Wang, Nanoscale phase separation, cation ordering, and surface chemistry in pristine $Li_{1.2}Ni_{0.2}Mn_{0.6}O_2$ for Li-ion batteries, Chem. Mater. 25 (2013) 2319-2326.

[47] A. Devaraj, M. Gu, R. Colby, P. Yan, C.M. Wang, J.M. Zheng, J. Xiao, A. Genc, J.G. Zhang, I. Belharouak, D. Wang, K. Amine, S. Thevuthasan, Visualizing nanoscale 3D compositional fluctuation of lithium in advanced lithium-ion battery cathodes, Nat. Commun. 6 (2015) 8014.

[48] D.W. Shin, C.A. Bridges, A. Huq, M.P. Paranthaman, A. Manthiram, Role of cation ordering and surface segregation in high-voltage spinel $LiMn_{1.5}Ni_{0.5-x}M_xO_4$ (M=Cr, Fe, and Ga) cathodes for lithium-ion batteries, Chem. Mater. 24 (2012) 3720-3731.

[49] C.G. Van de Walle, J. Neugebauer, First-principles calculations for defects and impurities: Applications to III-nitrides, J. Appl. Phys. 95 (2004) 3851-3879.

[50] G.G. Amatucci, C.N. Schmutz, A. Blyr, C. Sigala, A.S. Gozdz, D. Larcher, J.M. Tarascon, Materials effects on the elevated and room temperature performance of $CLiMn_2O_4$ Li-ion batteries, J. Power Sources 69 (1997) 11-25.

[51] N.P.W. Pieczonka, Z. Liu, P. Lu, K.L. Olson, J. Moote, B.R. Powell, J.-H. Kim, Understanding transition-metal dissolution behavior in $LiNi_{0.5}Mn_{1.5}O_4$ high-voltage spinel for lithium ion batteries, J. Phys. Chem. C 117 (2013) 15947-15957.

[52] D. Tang, Y. Sun, Z. Yang, L. Ben, L. Gu, X. Huang, Surface structure evolution of $LiMn_2O_4$ cathode material upon charge/discharge, Chem. Mater. 26 (2014) 3535-3543.

[53] L. Jaber-Ansari, K.P. Puntambekar, S. Kim, M. Aykol, L. Luo, J. Wu, B.D. Myers, H. Iddir, J.T. Russell, S.J. Saldaña, R. Kumar, M.M. Thackeray, L.A. Curtiss, V.P. Dravid, C. Wolverton, M.C. Hersam, Suppressing manganese dissolution from lithium manganese oxide spinel cathodes with single-layer graphene, Adv. Energy Mater. 5 (2015) 1500646.

[54] R. Benedek, M.M. Thackeray, J. Low, T. Bučko, Simulation of aqueous dissolution of lithium manganate spinel from first principles, J. Phys. Chem. C 116 (2012) 4050-4059.

Table 1. Lattice sites for the Ni replacement of Mn in the $MgMn_2O_4$ and calculated relative

total energies (eV).

	Sites			Configurations							
#	x	y	Z	1	2	3	4	5	6	7	8
1	0.125	0.625	0.875							Ni	Ni
2	0.375	0.875	0.875								
3	0.125	0.875	0.625	Ni	Ni	Ni		Ni		Ni	
4	0.375	0.625	0.625				Ni		Ni		Ni
5	0.625	0.125	0.875	Ni	Ni	Ni	Ni	Ni	Ni		
6	0.875	0.375	0.875								
7	0.625	0.375	0.625								
8	0.625	0.625	0.375								
9	0.125	0.125	0.375	Ni	Ni		Ni		Ni		Ni
10	0.875	0.125	0.625								
11	0.375	0.375	0.375			Ni		Ni		Ni	
12	0.375	0.125	0.125	Ni				Ni	Ni	Ni	Ni
13	0.125	0.375	0.125								
14	0.875	0.875	0.375								
15	0.625	0.875	0.125								
16	0.875	0.625	0.125		Ni	Ni	Ni				
	ΔE_{tot}			0.34	0.04	0.00	0.01	0.50	0.03	0.09	0.46

Table 2. Calculated lattice constants of spinel-$MgMn_2O_4$ and $MgNi_{0.5}Mn_{1.5}O_4$ and k-points

used in the simulations

	Space group		Lattice parameters			K-points		
			a (Å)	b (Å)	c (Å)	i	j	k
$MgMn_2O_4$	Fd-3m	FM	8.56	8.56	8.56	4	4	4
		AFM	8.31	8.31	9.10	4	4	4
$MgNi_{0.5}Mn_{1.5}O_4$	P4$_3$32	FM	8.50	8.50	8.50	4	4	4
		AFM	8.48	8.50	8.50	4	4	4

Table 3. Surface energies (in J/m^2) for the (001), (110), and (111) facets of MgMn$_2$O$_4$ and MgNi$_{0.5}$Mn$_{1.5}$O$_4$, respectively. The number of atoms (N) used are also given.

Facets	Termination	N	E_{surf}	Termination	N	E_{surf}
		MMO		**MNMO**		
(001)	Mg	142	0.08	Mg	142	0.08
	Mn/O	138	0.10	Mn/Ni/O	138	0.11
(110)	Mn/O	236	0.13	Mn/O	236	0.13
	Mg/Mn/O	212	0.13	Mg/Mn/Ni/O (I)	212	0.13
				Mn/Ni/O	180	0.14
				Mg/Mn/Ni/O(II)	212	0.13
(111)	Mn(I)	292	0.31	Mn/Ni(I)	292	0.29
	O(I)	212	0.22	O(I)	268	0.25
	O(II)	268	0.15	O(II)	324	0.19
	Mg(I)	236	0.23	Mg(I)	236	0.22
	Mn(II)	284	0.11	Mn/Ni(II)	284	0.11
	Mg(II)	276	0.11	Mg(II)	276	0.12

Table 4. The distances between the first layers and second layers before and after relaxation, respectively.

| Facets	Termination	Interlayer spacing (Å) Before	After	Termination	Interlayer spacing (Å) Before	After
		MMO			**MNMO**	
(001)	Mn/O	1.17	1.03	Mn/Ni/O	1.17	0.95
(110)	Mn/O	1.60	1.44	Mn/O	1.59	1.49
	Mg/Mn/O	1.42	1.37	Mg/Mn/Ni/O (I)	1.41	1.37
				Mn/Ni/O	1.66	1.51
				Mg/Mn/Ni/O(II)	1.48	1.35
(111)	Mn(I)	1.03	1.02	Mn/Ni(I)	1.04	1.02
	O(II)	1.23	0.84	O(II)	1.21.	0.95
	Mg(II)	0.66	0.56	Mg(II)	0.64	0.54

Figure captions:

Figure 1: The crystal structures of (a) MMO (Fd-3m) and (b) MNMO (P4$_3$32). The purple octahedrons represent Mn atoms, and the grey octahedrons represent Ni replacement. The Mg and O atoms are depicted using the orange and red balls, respectively.

Figure 2: Surface energies as a function of slab thickness. Surfaces of MMO and MNMO are denoted with real and dash lines, respectively.

Figure 3: The atomic overall arrangement along the [001], [110] and [111] crystal orientation, respectively. The (a), (b) and (c) severally represent the atomic layer sequences along the [001], [110], [111] crystal orientation for MNMO. The (d), (e) and (f) severally represent the atomic layer sequences along the [001], [110], [111] crystal orientation for MMO, respectively.

Figure 4: Atomistic configurations of MNMO surfaces before and after relaxations. (a)/(b) unrelaxed/relaxed (001) surface with Mg-termination; (c)/(d) unrelaxed/relaxed (111) surface with Mg(I)-layer; (e)/(f) unrelaxed/relaxed (111) surface with O(I)-layer; (g)/(h) unrelaxed/relaxed (111) surface with Mn/Ni(II)-layer.
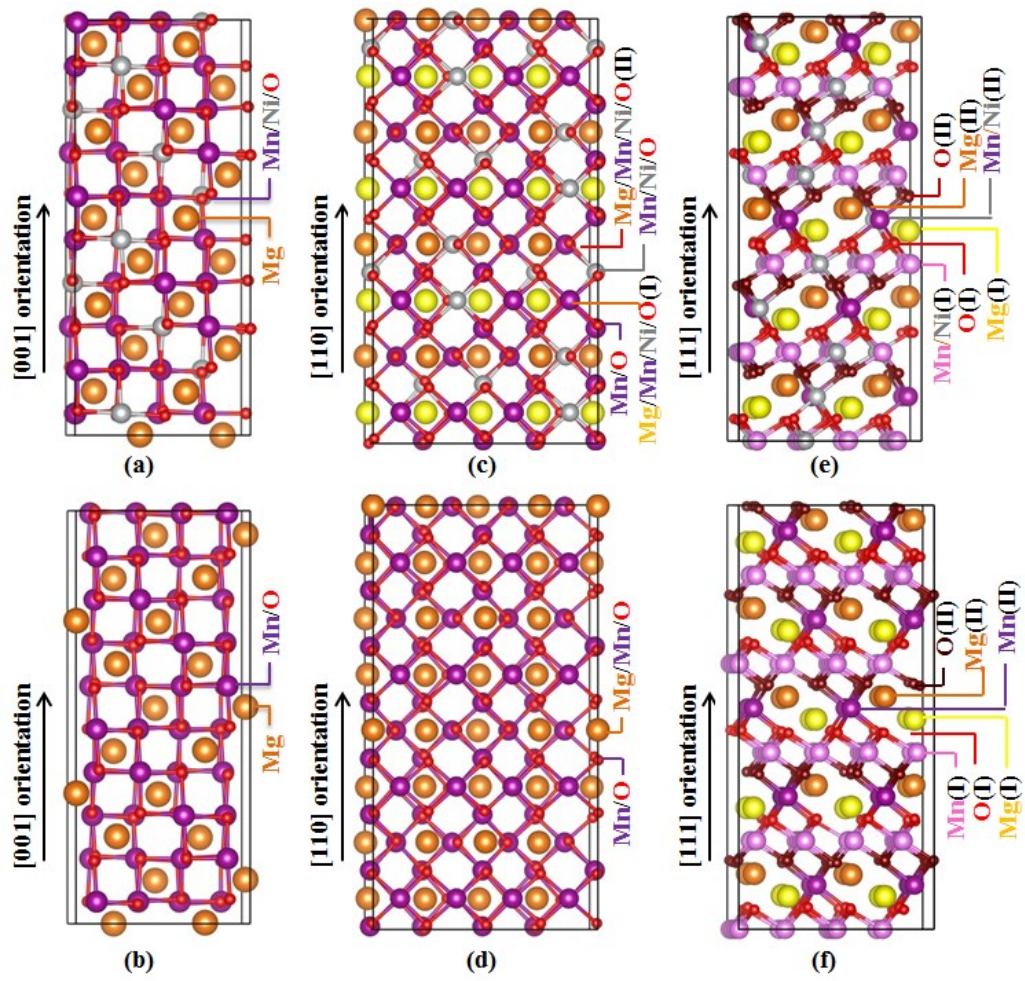
Figure 5: Formation energies of a Ni atom replacement of a Mn atom in the MMO slabs.
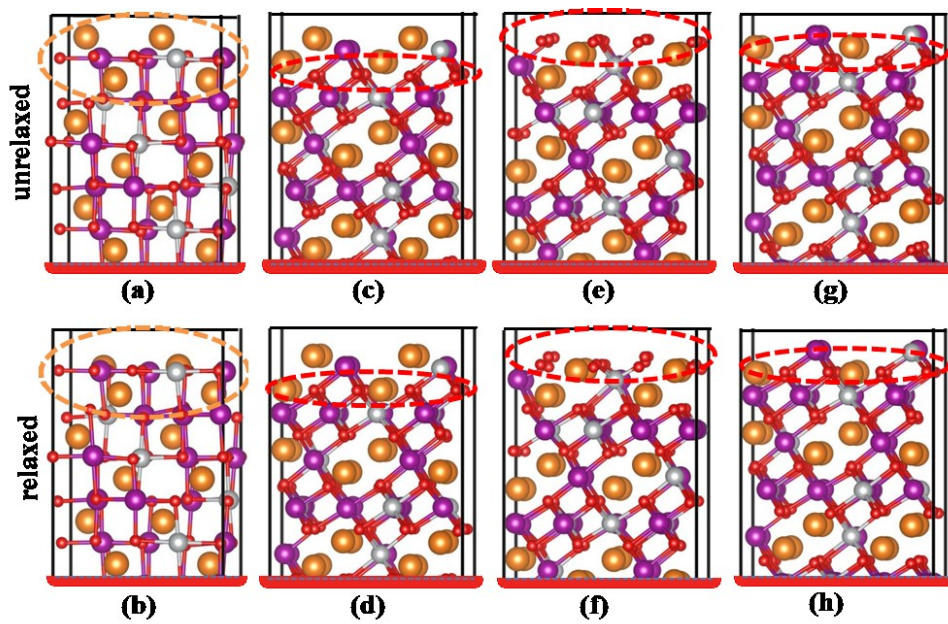
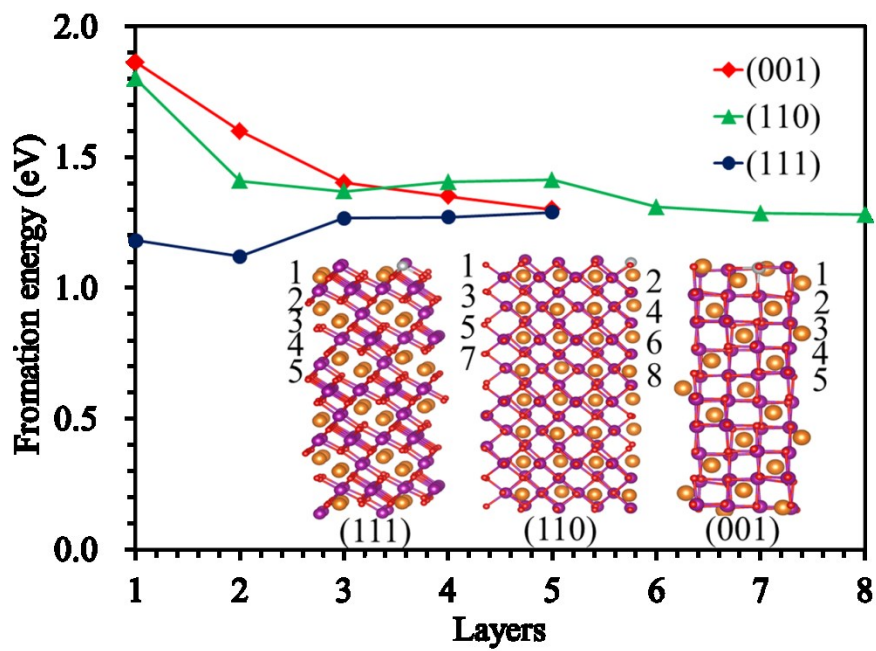(a)   (b)
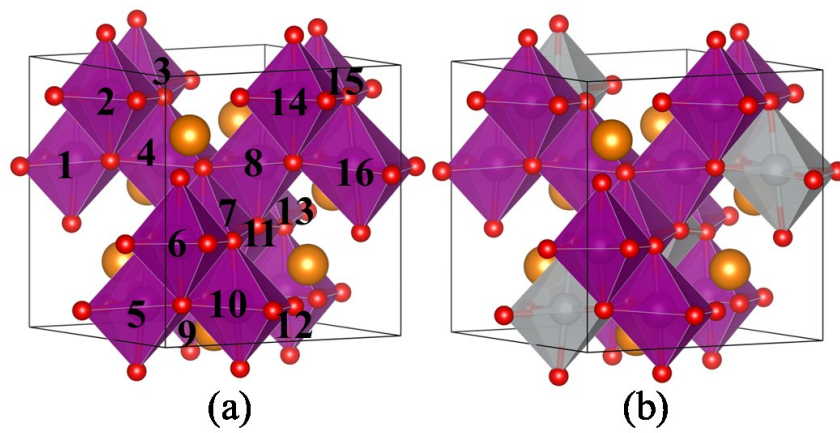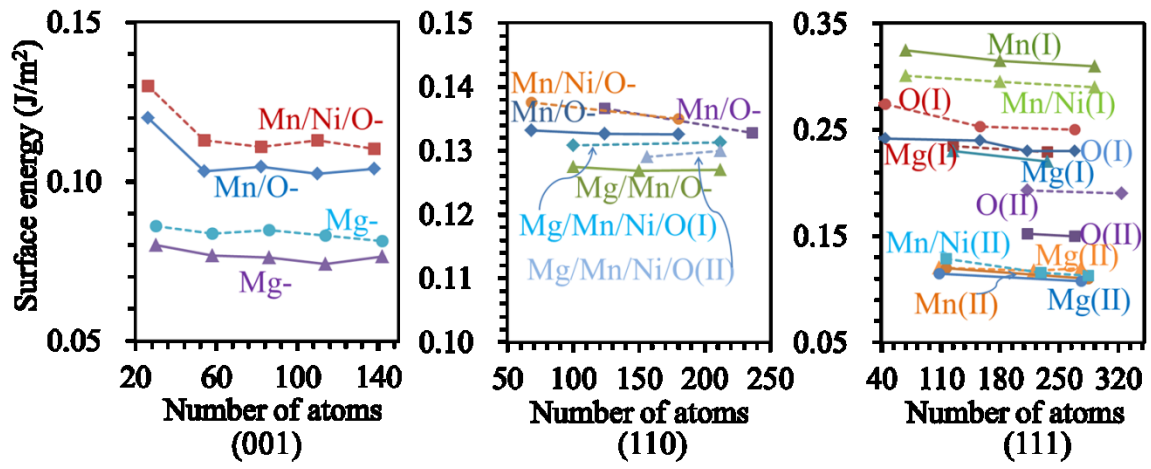
W.Jin et al. Figure 1

W. Jin et al. Figure 2

W.Jin et al. Figure 3

W.Jin et al. Figure 4

W.Jin et al. Figure 5